Discover Applied Sciences

RESEARCH Open Access

Simultaneous photodegradation of acetaminophen and caffeine using a ZnO/CeO_2/g-C_3N_4 nanocomposite

Judith Chebwogen[1,2], Francis W. Nyongesa[2], Julius M. Mwabora[2] and Patrick G. Ndungu[1*]

*Correspondence:
Patrick G. Ndungu
patrick.ndungu@up.ac.za
[1]Department of Chemistry, University of Pretoria, Private Bag X20, Hartfield 0028, South Africa
[2]Department of Physics, University of Nairobi, P.O. Box 30197-00100, Nairobi, Kenya

Abstract

Semiconductor coupling delivers improved efficiency in photocatalytic water treatment. This study investigated the simultaneous photocatalytic degradation of acetaminophen and caffeine using a hydrothermally fabricated ZnO/CeO_2/g-C_3N_4 nanocomposite. The nanocomposite physical-chemical properties were investigated using powder X-ray diffraction (PXRD), scanning electron microscopy (SEM), Transmission Electron Microscopy (TEM), photoluminescence, UV-Vis spectroscopy and nitrogen adsorption characterization techniques. A reduction in band gap from 3.10 eV to 2.65 eV and an increase in specific surface area from 10.039 m^2/g and 34.364 m^2/g for ZnO and ZnO/CeO_2/g-C_3N_4 respectively was observed. The SEM and TEM studies demonstrated a good interaction between ZnO, CeO_2 and g-C_3N_4, while photoluminescence confirmed enhanced charge transfer with the formation of the nanocomposite. The ternary nanocomposites exhibited higher photocatalytic efficiencies than pristine semiconductors, with 70% and 40% of 2 µg/mL acetaminophen and caffeine degraded, respectively, by 1.5 gL^{-1} of the ZnO/CeO_2/g-C_3N_4 nanocomposite under UV-A irradiation. The synergistic properties of the nanocomposite make it a promising material for further study and application in environmental remediation.

Keywords Ternary nanocomposite, Photodegradation, Pharmaceuticals, Environmental remediation

1 Introduction

The amount of solar energy reaching the Earth's surface far exceeds global energy needs by several orders of magnitude, making it an attractive source for applications like photocatalytic water decontamination and hydrogen production through water splitting. Extensive research on water contamination reveals that industrialization, population growth and urbanization are among the major contributors to water pollution [1, 2]. Additionally, hospital effluents, municipal wastewater, sewage leaks, improper drug disposal and agricultural practices introduce contaminants, including pharmaceuticals, into surface water [3]. Poor sanitation, particularly in developing countries, can lead to

human waste containing metabolized by-products or unmetabolized pharmaceuticals entering into water bodies [4]. While pharmaceuticals are essential for human and animal well-being, their presence, and that of their metabolites, in water bodies may have adverse health effects on both humans and aquatic life [5]. These pharmaceutical compounds include antibiotics, antivirals, analgesics, nonsteroidal drugs, hormonal medications or anti-inflammatory drugs. Although they can be detected in concentrations as low as ng L^{-1} to μg L^{-1} in water [6], continuous exposure may pose long-term risks to living organisms and the ecosystem [7].

Acetaminophen used for fever and pain relief is readily available over the counter and enters the environment and various water sources through human waste, industrial effluents, and domestic wastewater [8]. It has been detected and quantified in hospital wastewater, sewage sludge, groundwater and surface waters [9]. Concentrations up to 65 μg L^{-1} of acetaminophen have been detected in wastewater and it has been found to degrade to levels below 10 μg L^{-1} using conventional water treatment techniques [10]. It is part of a growing list of emerging contaminants for which standard regulations are not well-defined and that can have detrimental effects on human health and the environment [11] highlighting the need for complete removal from water. Caffeine found in various beverages and foods acts as a stimulant for the nervous, respiratory and circulatory systems [12]. Its frequent detection in groundwater, surface water, wastewater treatment plant effluents and soil are attributed to its high solubility and global consumption. Concentrations as high as 230 μg L^{-1} of caffeine have been detected in surface streams potentially sourced from coffee shops, untreated wastewater and industrial discharge. It has been regarded as an anthropogenic marker for surface water contamination [13].

Photocatalysis is an advanced oxidation process that has been extensively studied for environmental remediation and water decontamination [14, 15]. It shows significant potential for completely degrading emerging contaminants through highly oxidative species such as hydroxyl (•OH) and superoxide ($O_2^{\bullet-}$) radicals [16]. Although zinc oxide (ZnO) has been used in photocatalytic applications, its effectiveness is limited by its inability to absorb visible light [17], insufficient surface area and charge recombination [18]. Strategies such as non-metal or metal doping and heterojunction construction with other semiconductors have been explored to enhance absorption and charge separation in ZnO. Among these approaches, constructing heterojunctions has proven particularly effective [19] due to the synergistic properties arising from the interaction between the semiconductors.

Binary heterojunctions between ZnO and narrow bandgap semiconductors such as CeO_2, Fe_2O_3, WO_3 and g-C_3N_4 improve radiation absorption through band gap reduction and promote charge separation [20]. Ceria (CeO_2), which is primarily used for gas sensors, energy storage and catalysis, has excellent redox capabilities and is characterized by a high density of oxygen vacancies [21]. Its band gap, ranging from 2.8 to 3.1 eV, allows it to be activated by both visible and ultraviolet radiation [22] making it suitable for enhancing radiation absorption in wide bandgap semiconductors [23]. Additionally, its 4f orbital is incompletely filled leading to the valence variations of Ce^{3+} and Ce^{4+}. The redox couple cycle (Ce^{3+}/Ce^{4+}) enhances the separation of photogenerated charge and facilitates interfacial charge transfer [24]. A binary nanocomposite of ZnO and CeO_2 facilitates efficient charge separation due to favourable band alignment, reducing charge recombination. Furthermore, enhanced light absorption contributes to improved

photocatalytic efficiency [25]. Graphitic carbon nitride (g-C_3N_4) is a metal-free semiconductor that is active under visible light and has been utilized in CO_2 photoreduction, water splitting, and the photocatalytic mineralization of organic pollutants [26, 27]. Its advantages include visible light activity, chemical and thermal stability, low cost, an attractive electronic structure, a large surface area, and abundant binding sites [28]. However, despite its photocatalytic properties, its efficiency is limited by high charge recombination and a low quantum yield [29]. Forming a binary nanocomposite with ZnO enhances charge separation and broadens the spectral response due to their overlapping band structures, improving photodegradation efficiency [30].

While binary nanocomposites enhance efficiency, ternary nanocomposites have recently gained attention due to their superior performance which is linked to delayed recombination through charge transfer between the two semiconductor heterojunctions [31]. Numerous studies have assessed the photocatalytic performance of g-C_3N_4-based ternary nanocomposites. For instance, g-C_3N_4/CeO_2/TiO_2 [32], Gd-ZnO-g-C_3N_4 [27], and g-C_3N_4/ZnO/AgCl [33] demonstrated improved efficiency in degrading organic contaminants under visible and solar light irradiation. Additionally, a ternary nanocomposite composed of ZnO, CeO_2 and g-C_3N_4 is promising due to its well-matched overlapping band structures [30]. Research on g-C_3N_4/CeO_2/ZnO [34] and zeolite-supported g-C_3N_4/ZnO/CeO_2 [35] nanocomposites has revealed good stability and improved performance in the photodegradation of methylene blue attributed to three-level charge transfer, increased active sites and a reduced band gap. However, to our knowledge, the performance of this ternary nanocomposite in the simultaneous photodegradation of acetaminophen and caffeine has not been reported.

In this study, we hydrothermally synthesized a ZnO/CeO_2/g-C_3N_4 nanocomposite with varying masses of g-C_3N_4. We investigated its structural, optical, morphological and textural properties and evaluated its performance in the simultaneous photodegradation of acetaminophen and caffeine. We also examined the nanocomposite's stability over four cycles. Our findings indicated that a composite of ZnO, CeO_2 and g-C_3N_4 has improved properties and enhanced photocatalytic performance than the pristine components. Additionally, the nanocomposite remained stable after four cycles.

2 Chemicals and methods

2.1 Chemicals

Zinc acetate dihydrate (99%), cerium (III) nitrate hexahydrate (99%), citric acid (99%), ethanol ($\geq$ 95%), sodium hydroxide (extrapure AR), melamine (99%), acetaminophen (98%–102%) and caffeine ($\geq$ 99.5%) were all purchased from Sigma Aldrich and used as purchased.

2.2 Preparation of the catalysts

Graphitic carbon nitride (g-C_3N_4) was prepared by heat-treating melamine. Approximately 15 g of melamine was placed in a 100 mL ceramic crucible and heated in a muffle furnace at 550 °C for 5 h in air. After heating, the furnace was allowed to cool to room temperature and the resulting yellow powder was collected and used for further processing.

The ZnO/CeO_2 nanocomposite was synthesized using a 0.2 M zinc acetate dihydrate solution, prepared in a solvent mixture of water and ethanol (in a volume ratio of 5:1). In

a typical procedure, 2 g of citric acid was added to the 0.2 M zinc acetate dihydrate solution with stirring, followed by the addition of 1.3 g of cerium (III) nitrate hexahydrate. The mixture was stirred for 30 min. A glass pipette was used to add 0.1 M of sodium hydroxide dropwise to adjust the solution pH to 13. The solution was then poured into a Teflon-lined autoclave and heated for 17 h at 150 °C in a preheated oven. After cooling to ambient temperature, the powder was recovered by centrifugation, dried overnight at 70 °C in an oven, and calcined for 3 h at 400 °C in a muffle furnace under air. A Yellow powder with a ZnO: CeO_2 mass ratio of 2:1 was obtained and designated as ZnO/CeO_2. Pristine ZnO was synthesized using a similar procedure excluding adding cerium (III) nitrate hexahydrate. In contrast, the pristine CeO_2 was prepared using the same method using cerium (III) nitrate hexahydrate as the precursor.

To prepare the $ZnO/CeO_2/g\text{-}C_3N_4$ ternary nanocomposite, a specific mass of the prepared $g\text{-}C_3N_4$ was first dispersed in 10 mL of distilled water using an ultrasonic water bath. This dispersion was then mixed with a solution of zinc acetate dihydrate and cerium (III) nitrate hexahydrate, prepared according to the method used for making the ZnO/CeO_2 samples. The resulting mixture was transferred into a Teflon-lined autoclave and heated for 17 h at 150 °C in a preheated oven. After cooling, the product was washed with distilled water and ethanol, dried overnight at 70 °C in an oven and then calcined for 3 h at 400 °C. Samples prepared with 1.0 g of $g\text{-}C_3N_4$ were labelled as $ZnO/CeO_2/1.0CN$, those with 1.5 g were labelled as $ZnO/CeO_2/1.5CN$, and samples prepared with 2.0 g were labelled as $ZnO/CeO_2/2.0CN$. Figure 1 illustrates the synthesis process of the photocatalyst.

2.3 Characterization of the catalysts

The XRD patterns used to determine the crystallographic phases and purity of the powder samples were obtained using PANalytical X'Pert X-ray diffractometer with a Cuk α radiation, operated at 40 mA and 45 kV. The scans were conducted over a 2θ range of 5° to 80° at a scanning rate of 0.008° for 10 s each. Scanning Electron Microscopy (SEM) was performed with a FEGSEM Zeiss 540 Ultra instrument. The phase composition and structural properties of the samples were analyzed using a FEGTEM Jeol 2100 Transmission Electron Microscope. Textural characterization was conducted using Quantachrome's Autosorb iQ instrument, with the samples degassed for 10 h at 200 °C under vacuum before analysis. Fourier Transform Infrared Spectroscopy (FTIR) was performed

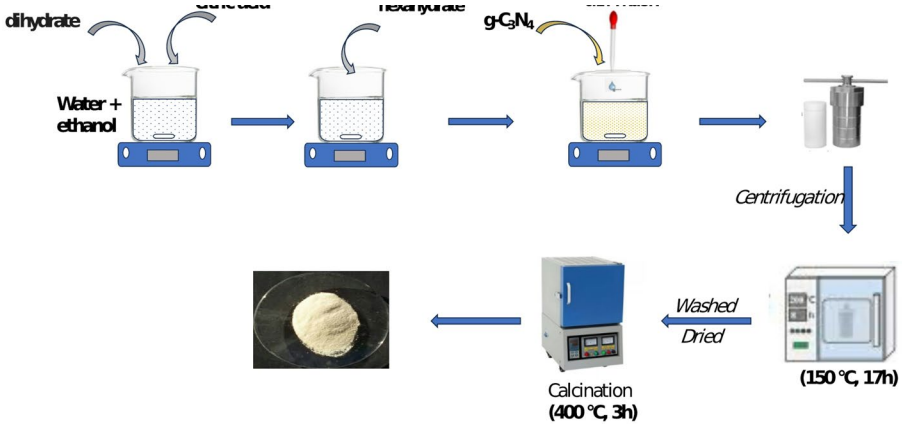

Fig. 1 A schematic of the synthesis process

on KBr-prepared sample pellets using a Bruker ALPHA II spectrophotometer. For photoluminescence studies, a Horiba Jobin Yvon Fluoromax-4 spectrofluorometer was utilized and a Cary UV-visible spectrophotometer was used to assess potential exciton transitions in water-dispersed samples.mX-ray photoelectron spectroscopy (XPS) analysis, was done using a Thermo ESCAlab 250Xi. Operational parameters were, X-Ray was generated from monochromatic Al Kα at 1486.7 eV, the X-ray power was 300 W, the X-ray spot size was 900 µm, pass Energy (Survey) 100 eV, pass Energy (Hi Res) 20 eV, and operating pressure was $< 10^{-8}$ mBar.

2.4 Photodegradation of acetaminophen and caffeine

The photocatalytic performance of the samples was evaluated in acetaminophen and caffeine degradation under UV-A irradiation. In a typical run, a 50 mL mixture of 10 µg/mL of both acetaminophen and caffeine along with 0.5 g/L catalyst was magnetically stirred for 30 min in the dark to achieve adsorption-desorption equilibrium. A 100 W UV-A source (UVA Frosted Daylight Reptile Heat Lamp, 100 W, purchased from Takealot™, South Africa) irradiated the mixture for 130 min. A 0.5 mL aliquot of the mixture was withdrawn at 30-minute intervals using a 3.0 mL syringe, filtered through a 0.45 µm PFTE membrane syringe filter and diluted by transferring it to a 5.0 mL volumetric flask and filling it with distilled water. Liquid Chromatography Mass Spectrometry (LCMS) was conducted to quantify the concentrations. Experiments were done in triplicate. A detailed description of the solvents used, detection and quantification of the samples is provided in the supplementary information section. The degradation efficiency and rate constants of the samples were determined using the relations shown in Eqs. 1 and 2. The influence of factors such as initial concentration, pH and the quantity of catalyst on photocatalytic efficiency was evaluated. Sample recyclability and the scavenger effect were also examined.

$$\% \, Degradation = \frac{C_o - C_t}{C_o} \times 100\% \tag{1}$$

$$kt = -ln\frac{[C_t]}{[C_0]} \tag{2}$$

3 Results and discussion

3.1 XRD patterns

Figure 2 displays the diffraction pattern of the samples. The ZnO pattern exhibits peaks at 31.74°, 34.40°, 36.23°, 47.52°, 56.58°, 62.85°, 66.37°, 67.94°, 69.08°, 72.57° and 76.96° (Fig. 2(a)). These peaks correspond to the (100), (002), (101), (102), (110), (103), (200), (112), (201), (004) and (202) lattice planes, confirming a hexagonal wurtzite structure consistent with previous studies [23, 36, 37]. The sharpness of the peaks confirms its crystallinity. Also, the CeO_2 diffraction pattern displayed peaks at 28.45°, 32.99°, 47.43°, 56.34°, 59.04°, 69.43°, 76.65° and 79.06° (Fig. 2 (a)), which are associated with the (111), (002), (220), (311), (222), (400), (331) and (420) planes, indicating its cubic fluorite structure [38, 39]. The g-C_3N_4 pattern (Fig. 2 (b)) reveals two peaks at 13.24° and 27.39° corresponding to (100) and (002) planes [34]. The prominent peak at (002) indicates the periodic stacking of aromatic C-N units [40] while the (001) peak suggests in-plane

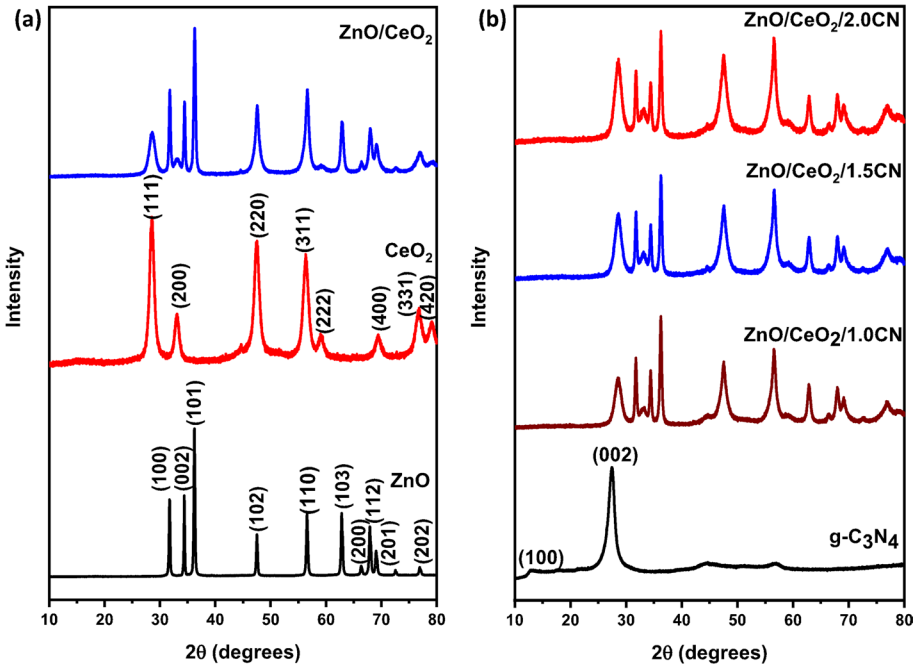

Fig. 2 In (**a**), the XRD patterns of the ZnO, CeO_2 and ZnO/CeO_2 samples are presented, and in (**b**) the XRD patterns for the samples g-C_3N_4, ZnO/CeO_2/1.0CN, ZnO/CeO_2/1.5CN and ZnO/CeO_2/2.0CN are presented

Table 1 Computed crystal sizes, cell volumes, lattice parameters and lattice planes using the (100) and (002) reflections for the indicated samples

Catalyst	Crystal size (nm)	Lattice planes				Lattice parameters		Cell volume $(Å)^3$
		100		002		a	c	
		2 θ	FWHM	2 θ	FWHM			
ZnO	26.00	31.74	0.250	34.40	0.207	3.251	5.207	47.66
CeO_2	6.32	-	-	-	-	5.421	-	159.31
g-C_3N_4	5.24	-	-	-	-	-	-	-
ZnO/CeO_2	12.63	31.78	0.333	34.45	0.287	3.247	5.201	47.49
ZnO/CeO_2/1.0CN	11.33	31.76	0.345	34.42	0.325	3.249	5.206	47.59
ZnO/CeO_2/1.5CN	11.40	31.78	0.333	34.43	0.318	3.247	5.203	47.51
ZnO/CeO_2/2.0CN	11.21	31.78	0.344	34.42	0.336	3.248	5.205	47.55

triazine units packing [41]. The interplanar distance calculated from the (002) peak is 0.325 nm, similar to previous reports [42].

In the ternary nanocomposite (Fig. 2 (b)), the characteristic peaks of ZnO, CeO_2, and g-C_3N_4 were observed in the diffraction pattern, albeit with some overlaps. Specifically, an overlap between the (111) plane of CeO_2 and (002) plane of g-C_3N_4 was noted. The intensity of the resulting peak increased with the amount of g-C_3N_4 in the samples as expected. Additionally, the superposition of the ZnO (102) and (110) planes with the CeO_2 (220) and (311) peaks respectively resulted in a stronger peak in the nanocomposites, confirming the presence of the components in the prepared nanocomposites [43]. The coupling of ZnO with CeO_2 caused a slight shift to higher 2 θ angles as presented in Table 1 indicating a good interaction while ZnO peaks broadened upon nanocomposite formation indicating decreased crystallite size [19]. This was further supported by the crystallite sizes calculated using the Debye-Scherrer Eq. (3) [44]. In photocatalysis,

a reduction in crystal size has been reported to suppress charge recombination and enhance the energy of photogenerated radicals, thereby improving performance [45]. The ZnO lattice parameters were determined using Eqs. (4) and (5) [46], while the lattice parameters of CeO_2 were calculated using Eq. (6) due to its cubic structure [47]. The unit cell volumes of the samples were determined using Eq. (7) [48]. The decrease in the unit cell volume in the nanocomposites compared to pristine ZnO and CeO_2 was associated with the decreased lattice parameters and suggests the interaction of the components in the nanocomposite [49, 50].

$$D = \frac{k\lambda}{\beta\ cos\theta} \tag{3}$$

$$a = \sqrt{\frac{1}{3}}\frac{\lambda}{sin\theta} \tag{4}$$

$$c = \frac{\lambda}{sin\theta} \tag{5}$$

$$a = \left[d^2\ \left(h^2 + k^2 + l^2\right)\right]^{\frac{1}{2}} \tag{6}$$

$$V = \frac{\sqrt{3}}{2}a^2.c \tag{7}$$

where D represents the crystallite size in nm, k is a constant (0.89), β is the full-width half maximum (FWHM) in radians, is the X-ray wavelength (1.5406 Å), is half the Bragg's diffraction angle measured in radians.

3.2 FTIR spectra

The spectra showing stretching and vibrational peaks corresponding to various functional groups obtained from the FTIR analysis of KBr-prepared sample pellets are displayed in Fig. 3. The vibrational band observed at 470 cm^{-1} corresponds to the stretching of Zn-O bonds in ZnO [51] whereas that at 830 cm^{-1} is associated with the bending (deformation) vibration of water molecules [52]. The strong bands observed between 1430 cm^{-1} and 1550 cm^{-1} were associated with CO_3^{2-} vibration and bending modes [53] that may have originated from zinc acetate precursor, while the band at approximately 3400 cm^{-1} represents O-H stretching vibration. In the CeO_2 spectrum, a broad band attributed to the stretching vibration for Ce-O was observed at about 468 cm^{-1} [54]. Additionally, bands at 1042 cm^{-1}, 1350 cm^{-1} to 1538 cm^{-1} and 3400 cm^{-1} correspond to C-O, and COO- which may be from the citric acid used in synthesis and O-H respectively. In g-C_3N_4, the band located at 803 cm^{-1} corresponds to the out-of-plane bending of s-triazine units and confirms the presence of the g-C_3N_4 structure [55]. The broad band ranging from 1240 cm^{-1} –1640 cm^{-1} is related to carbon nitride rings stretching vibration, with C-N vibrations appearing at 1240 cm^{-1}, 1320 cm^{-1} and 1410 cm^{-1} and C = N stretching modes at 1560 cm^{-1} and 1640 cm^{-1} [56]. The N-H vibration was observed at about 3200 cm^{-1}. In the nanocomposites, the broad band between 3100 cm^{-1} and 3500 cm^{-1} is attributed to N-H vibration and O-H stretching vibrations originating from surface-adsorbed H_2O molecules [57]. Additionally, the broad bands between 450 cm^{-1} and 470 cm^{-1} were ascribed to Zn-O and Ce-O vibrations.

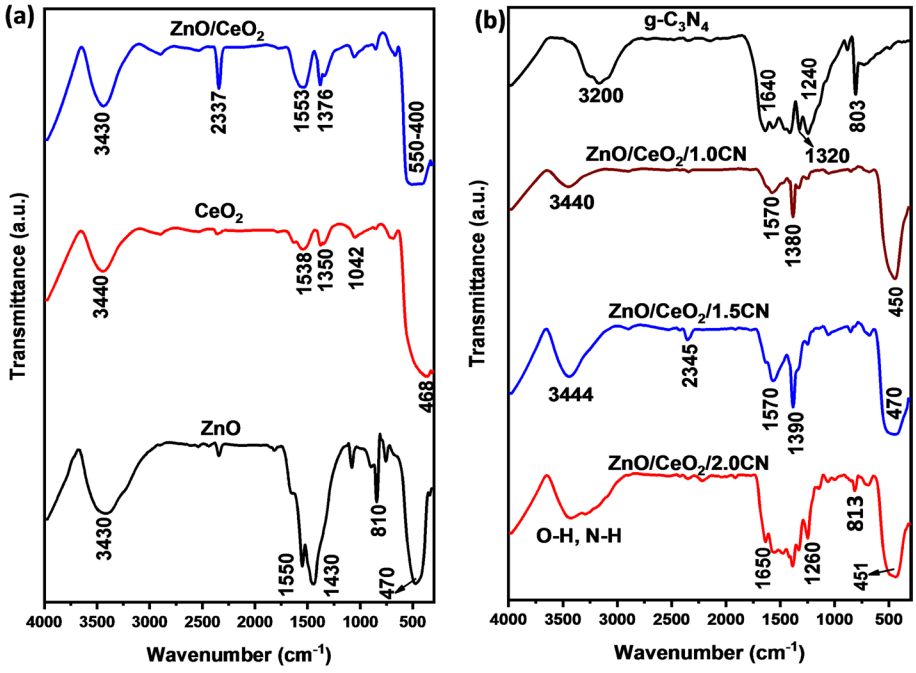

Fig. 3 Image (**a**) shows the FTIR spectra for ZnO, CeO_2 and ZnO/CeO_2 samples, and image (**b**) shows the FTIR spectra for the g-C_3N_4, ZnO/CeO_2/1.0CN, ZnO/CeO_2/1.5CN and ZnO/CeO_2/2.0CN samples

The intensities of C = N and C-N peaks increased with the rising g-C_3N_4 weight in the samples. The slight shift in the peaks associated with the triazine ring from 803 cm^{-1} to 813 cm^{-1} and C-N vibration from 1320 cm^{-1} to 1380 cm^{-1} indicated a good interaction between ZnO, CeO_2 and g-C_3N_4 consistent with XRD analysis. This promotes charge transfer in photocatalysis [58].

3.3 SEM analysis

Figure 4(a) shows the results of the SEM observations and indicates that flower-like microspheres formed from aggregated nanosheets. Magnified images reveal that the nanosheets were smooth and about 34 nm ± 1 thick. The formation of hydrothermally synthesized ZnO nanoflowers can be attributed to the effects of temperature and reaction time, with nanoflowers forming when the temperature and reaction time are increased to 150 °C and 15 h respectively [59]. In citric acid-assisted ZnO hydrothermal synthesis, a large quantity of negatively charged $[Zn(C_6H_5O_7)_4^{-12}]^{-10}$ complexes is generated, which preferentially adsorb to the [0001] positive polar plane, thereby limiting ZnO's anisotropic growth. This leads to the formation of disc-like nanostructures at low solution pH. An increase in the solution pH to 13 results in the aggregation of these nanostructures forming nanosheets [60] that later self-assemble to generate flower-like microspheres as the reaction time increases.

In Fig. 4(b), the sample formed aggregated spherical CeO_2 nanoparticles. The ZnO/CeO_2 synthesized sample favoured a similar morphology as the ceria, which was mainly spherical structures (see Fig. 4(c)). The formation of bulk g-C_3N_4 packed nanosheets was confirmed, and a typical SEM image is presented in Fig. 4(d). From Fig. 4(e), (f) and (g), it is evident that the ZnO/CeO_2 microspheres were supported on g-C_3N_4 nanosheets which were exfoliated through heat treatment during calcination or the hydrothermal process [61]. As expected, in Fig. 4(e), (f) and (g), the nanosheet morphology of the

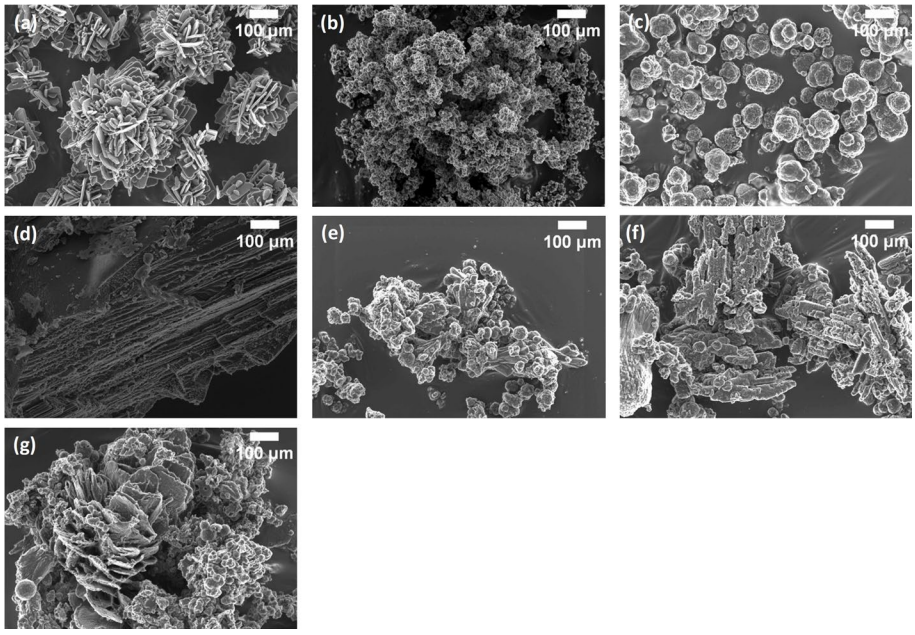

Fig. 4 SEM micrographs of the synthesized samples are shown in (**a**) ZnO, (**b**) CeO_2, (**c**) ZnO/CeO_2, (**d**) g-C_3N_4, (**e**) ZnO/CeO_2/1.0CN, (**f**) ZnO/CeO_2/1.5CN, and (**g**) ZnO/CeO_2/2.0CN

g-C_3N_4 nanomaterial becomes increasingly prominent as the mass of the g-C_3N_4 support is increased.

3.4 TEM analysis

TEM images of the synthesized samples are displayed in Fig. 5 where Fig. 5(a) confirms the aggregated nanosheets observed in SEM. Porous CeO_2 nanoparticles were formed as shown in Fig. 5(b) which got in between the ZnO nanosheets resulting in flower-shaped nanospheres formation as illustrated in Fig. 5(c). Figure 5(e), (f) and (g) show an interaction between g-C_3N_4 sheets and the flower-shaped nanostructures and confirm the increase in the nanosheets with the increase in g-C_3N_4 consistent with SEM.

3.5 BET isotherms

The pore size distribution and specific surface areas were analysed using the Brunauer-Emmett-Teller (BET) method. The ZnO samples displayed an H3 hysteresis loop with a Type V isotherm (Fig. 6 (a)) as per IUPAC guidelines [62]. The CeO_2 sample displayed a H4 hysteresis loop with a Type IV (a) isotherm, indicating that the material texture is mesoporous [62]. This was corroborated by the pore sizes between 2 nm and 50 nm [62]. obtained using the Barrett–Joiner–Halenda method on data from the desorption part of the isotherm, as presented in Table 2. The H3 hysteresis loop demonstrates that these pores were slit-shaped [63] and formed by the accumulation of flaky particles [64].

Table 2 provides information on the calculated BET surface areas and pore sizes of the various samples, and shows that the nanocomposites exhibited a higher surface area than pristine oxides. Also, the specific surface area increased with the introduction of g-C_3N_4 which was associated with the increase in the high surface g-C_3N_4 nanosheets as revealed by SEM analysis. A higher surface area is fundamental in photodegradation since it enhances the adsorption of pollutants. It also increases the number of active sites hence enhancing photocatalytic performance [65]. The reduction in the surface area of

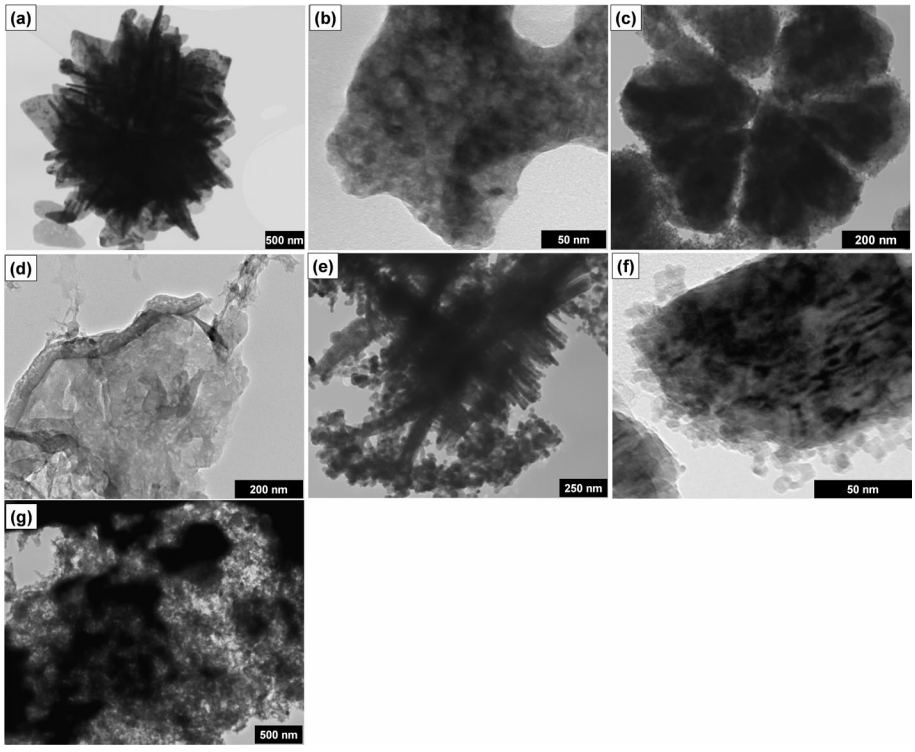

Fig. 5 TEM images of (**a**) ZnO, (**b**) CeO_2, (**c**) ZnO/CeO_2, (**d**) g-C_3N_4, (**e**) ZnO/CeO_2/1.0CN, (**f**) ZnO/CeO_2/1.5CN, and (**g**) ZnO/CeO_2/2.0CN

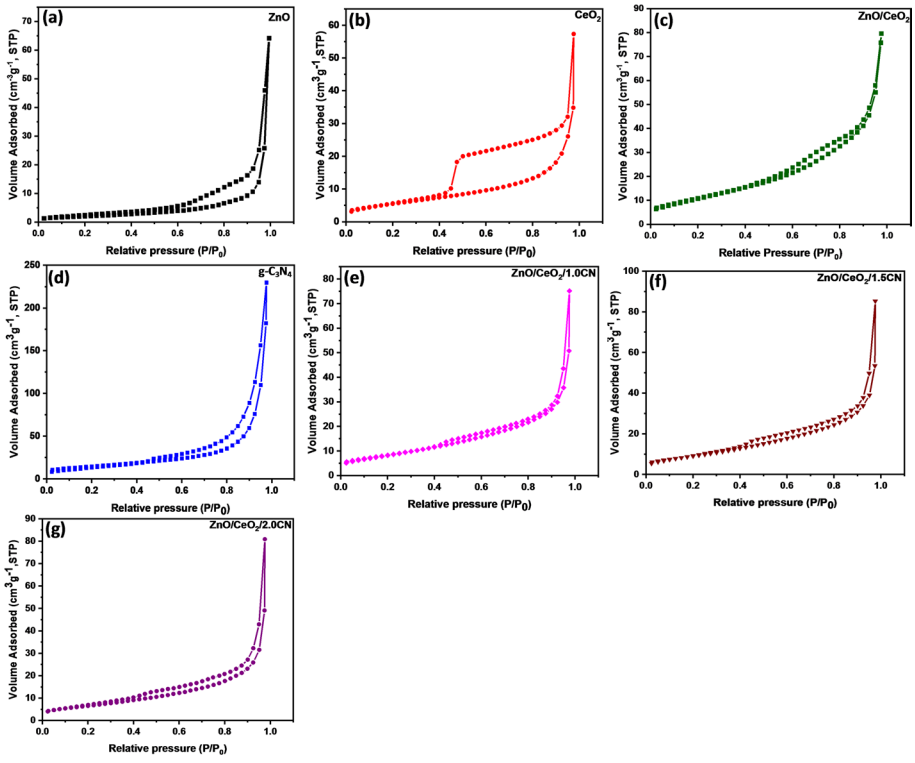

Fig. 6 The N_2 adsorption-desorption isotherms for ZnO (**a**), CeO_2 (**b**), ZnO/CeO_2 (**c**), g-C_3N_4 (**d**), ZnO/CeO_2/1.0CN (**e**), ZnO/CeO_2/1.5CN (**f**) and ZnO/CeO_2/2.0CN (**g**)

Table 2 The BET surface area and calculated pore sizes for the various samples synthesized

Sample	BET surface area (m^2/g)	Pore size (nm)
ZnO	10.04	3.145
CeO_2	20.52	3.716
ZnO/CeO_2	40.80	3.542
g-C_3N_4	51.29	3.719
ZnO/CeO_2/1.0CN	31.31	3.507
ZnO/CeO_2/1.5CN	34.36	3.531
ZnO/CeO_2/2.0CN	44.62	4.740

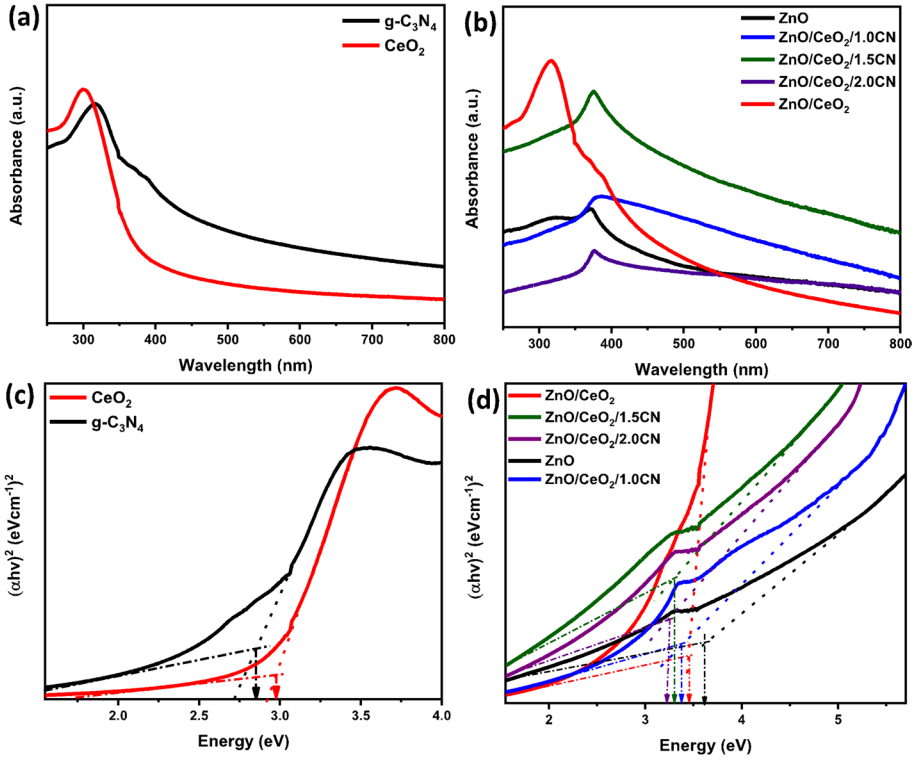

Fig. 7 Panel (**a**) presents the UV-Vis spectra of the CeO_2 and g-C_3N_4 samples. Panel (**b**) presents the UV-Vis spectra of the ZnO, ZnO/CeO_2, ZnO/CeO_2/1.0CN, ZnO/CeO_2/1.5CN, and the ZnO/CeO_2/2.0CN samples. The Tauc plots for the CeO_2 and g-C_3N_4 samples are presented in (**c**). In panel (**d**) the Tauc plots for ZnO, ZnO/CeO_2, ZnO/CeO_2/1.0CN, ZnO/CeO_2/1.5CN, and the ZnO/CeO_2/2.0CN samples are shown

the ternary nanocomposites compared to g-C_3N_4 and ZnO/CeO_2 binary nanocomposite may have resulted from agglomeration of the ZnO/CeO_2 particles on the g-C_3N_4 sheets reducing the exposed surface area as observed in SEM.

3.6 UV-Vis absorption

Figure 7(a) displays the absorption spectrum of the water-dispersed samples obtained by UV-Vis spectroscopy in the wavelength range 250 nm to 800 nm at room temperature. Well-defined absorption peaks were observed in all the samples. This indicated the transition of electrons to the conduction band minimum from the valence band maximum. A peak in an absorbance spectrum indicates that radiations of wavelengths lower than the absorption peak can excite electrons from the semiconductor conduction band [66]. ZnO and the nanocomposite spectra exhibited an absorption peak at about 375 nm that matched the ZnO hexagonal wurtzite structure [67]. The CeO_2 absorption

spectrum peaked at 300 nm and g-C_3N_4 at 316 nm. Slight shifts to higher wavelengths were observed in the nanocomposites indicating reduced energy required for charge excitation. The absence of other peaks in the spectra confirmed that the prepared samples were pure.

In photocatalytic reactions, the radiation energy utilized greatly depends on the semiconductor energy gap. Tauc plots based on Eq. (8) [68] used to evaluate the bandgaps of the samples are displayed in Figs. 7 (c) and (d).

$$(\alpha\, hv) = A(hv - E_g)^n \tag{8}$$

where hv is the photon energy, α the absorption coefficient, A is a constant, the band gap energy and n indicates the transition type equivalent to 2 for direct and band gap semiconductors.

The band gap energy was estimated by applying two linear fits above and below the fundamental peak, with their point of intersection giving the estimated value [69]. The values obtained were 3.60 eV, 2.98 eV, 2.85 eV, 3.46 eV, 3.37 eV, 3.30 eV and 3.22 eV for ZnO, CeO_2, g-C_3N_4, ZnO/CeO_2, ZnO/CeO_2/1.0CN, ZnO/CeO_2/1.5CN and ZnO/CeO_2/2.0CN respectively. This indicated a general decrease in the bandgap energies with nanocomposite formation, demonstrating effective interaction between the semiconductors [48]. Bandgap reduction is beneficial in photocatalytic applications since it enhances optical absorption hence the photoinduced carrier generation [70].

3.7 XPS analysis

XPS analysis was conducted to confirm the elemental composition and oxidation states. Figure 8(a) presents the full survey spectrum showcasing binding energy peaks that indicate the presence of Zn, Ce, O, N and C elements on the ZnO/CeO_2/1.5CN nanocomposite surface. The spectra displaying deconvoluted peaks of the individual elements are also shown in Fig. 8(b) to (f). Four peaks at 1021.9 eV, 1023.8 eV, 1045.0 eV and 1047.0 eV were observed in the Zn 2p spectrum. The first two correspond to $2p_{3/2}$ and the last two correspond to $2p_{1/2}$ and are all characteristic of the Zn^{2+} oxidation state [71, 72]. The deconvoluted peaks of Ce 3d illustrated in Fig. 8(c) show eight peaks at

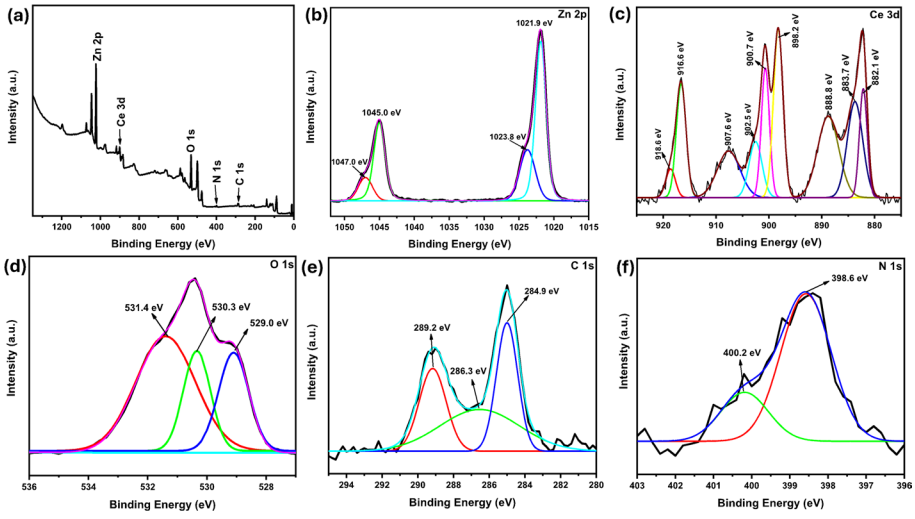

Fig. 8 Panel (**a**) presents the full survey XPS spectrum of ZnO/CeO_2/g-C_3N_4, (**b**) shows and deconvolution of Zn 2p (**b**), Ce 3 d (**c**), O 1 s (**d**), C 1 s (**e**) and N 1 s (**f**) spectrums

882.1 eV, 883.7 eV, 888.8 eV, 898.2 eV, 900.7 eV, 902.5 eV, 907.6 eV, 916.6 eV and 918.8 eV. Amongst these, the peaks at 883.7 eV and 902.5 eV are attributed to the Ce^{3+} oxidation state while the rest are attributed to the Ce^{4+} oxidation state [73], revealing mixed Ce^{3+} and Ce^{4+} valence states [74]. The O 1 s spectrum revealed three deconvoluted peaks. The first two at 529.0 eV, and 530.3 eV are associated with lattice oxygen (O_L) [75] representing the oxygen atoms bound in the metal oxide crystal structure, thus Ce-O and Zn-O bands and the other at 531.4 eV indicating surface hydroxyl oxygen (O_H) [76]. Additionally, the C 1 s spectrum exhibited three peaks at 284.9 eV, 286.3 eV and 289.2 eV indicating the presence of C-C, C-OH and C = O functional groups, consistent with FTIR analysis and confirming the interaction between carbon in g-C_3N_4 and the metal oxides. Furthermore, the N 1 s showed two peaks at 398.6 eV and 400.1 eV which confirmed the presence of C = N-C and C-N-H respectively, possibly originating from g-C_3N_4 triazine units [77].

3.8 Photoluminescence

Photoluminescence was performed under an excitation wavelength of 325 nm to investigate the recombination of charges and the nature of defects in the prepared samples [78]. A lower peak intensity in photoluminescence indicates an increased charge lifetime due to reduced recombination hence an enhanced transfer of charges. Figure 9(a) shows that charge recombination in g-C_3N_4 was high compared to the other samples, ascribed to its narrow band gap [79]. The g-C_3N_4 emission peak at approximately 445 nm was ascribed to band-to-band transition, equal to its band gap energy [80]. In Fig. 9(b), the ZnO spectrum exhibited a peak at 398 nm, corresponding to near band-edge emission, resulting in direct charge recombination [81]. Both metal oxides exhibited greater peak intensities than the nanocomposites. Coupling the nanocomposite with g-C_3N_4 resulted in lower peak intensities, indicating efficient separation of charges [35]. An exception was noted with the ZnO/CeO_2/2.0CN whose peak intensity was high. This was ascribed to the increase in the surplus defects that could be present in g-C_3N_4 which acted as recombination sites, especially with the increase in weight [82]. Otherwise, peak quenching evident in the nanocomposites stipulated enhanced photocatalytic activity [83] due to suppressed charge recombination as indicated by the XRD crystal size reduction. Among the ternary nanocomposites, ZnO/CeO_2/1.5CN exhibited the least peak intensity, suggesting improved charge separation, transport and expected enhanced

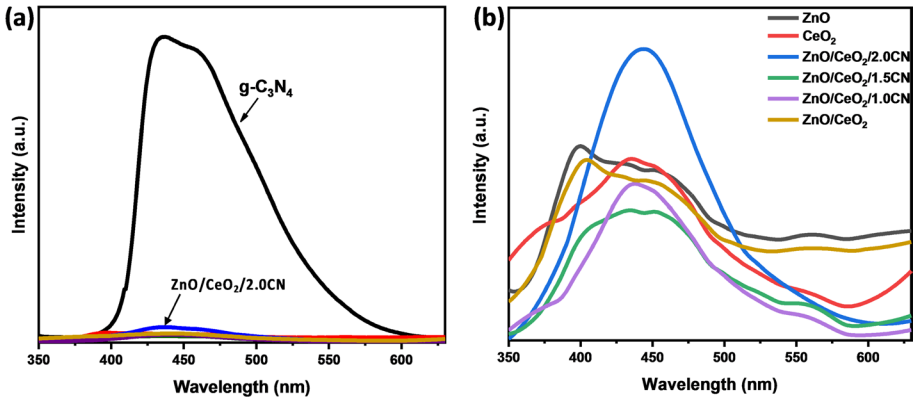

Fig. 9 Image (**a**) presents the photoluminescence spectra for all the synthesized samples, and image (**b**) compares the photoluminescence spectra of all the samples with the spectra for g-C_3N_4 removed

performance. It should be noted that the emission bands in the visible regions are consistent with the presence of defects such as oxygen vacancies in their structures [84], which allow for increased capture of the photo-generated electrons, producing radicals for photodegradation [85].

3.9 Photocatalytic degradation of acetaminophen and caffeine

The prepared samples were tested as photocatalysts in the degradation of a mixture of acetaminophen and caffeine, and the results are displayed in Fig. 10. These initial experiments used 10 µg/mL of the pharmaceuticals mixed with 1.0 g/L of the photocatalysts in a total volume of 50 mL of solution. The samples adsorbed a minimal amount of acetaminophen and caffeine molecules in the dark as shown in Fig. 10(a). Upon irradiation, a decrease in the concentration due to photodegradation was observed.

Figure 10 depicts that pure ZnO, CeO_2 and g-C_3N_4 can degrade both pharmaceuticals simultaneously, although with a relatively lower performance than the nanocomposites. In terms of the metal oxides, ZnO has a higher degradation activity than CeO_2, and the ZnO/CeO_2 nanocomposite has a higher activity than both single oxides. This observation may be attributed to the change in surface area as indicated in Table 2 where the ZnO/CeO_2 samples had a relatively higher surface area (40.80 m^2/g) versus the ZnO (10.04 m^2/g) and the CeO2 (20.52 m^2/g). A high surface area allows for more active sites for adsorption and reaction.

In terms of the g-C_3N_4 loading, there was an increase in photodegradation activity with increased loading. However, a further increase in the g-C_3N_4 load lowered the performance attributed to insufficient charge transfer as explained in Sect. 3.8. ZnO/CeO_2/1.5CN demonstrated a higher activity, which may be associated with its properties noted in the previous sections, including a narrow band gap that allows for greater light absorption and reduced charge recombination compared to the other samples. The photodegradation efficiencies and rate constants calculated using Eqs. (1) and (2) are displayed in Table 3. They were observed to be relatively lower in caffeine than in acetaminophen, likely due to the difference in their chemical structure [86].

3.9.1 Amount of catalyst

The effect of the amount of catalyst used in the photodegradation of the mixture of acetaminophen and caffeine was studied using varied amounts of catalyst (0.5 gL^{-1},

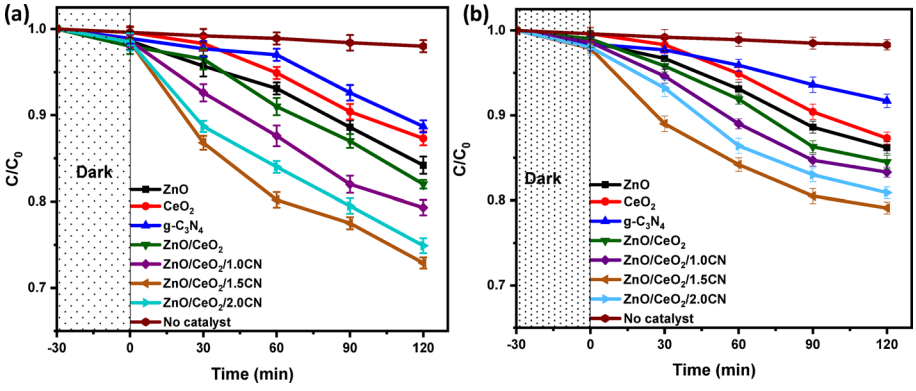

Fig. 10 Photocatalytic degradation of 10 µg/mL of (**a**) acetaminophen and (**b**) caffeine under UV-A irradiation using 1.0 g/L of the prepared sample catalyst and the natural pH of the solution

Table 3 Calculated acetaminophen and caffeine degradation efficiencies and rate constants using non-optimal initial conditions (natural pH of the solution, 10 µg/mL of acetaminophen and caffeine, and 1.0 g/l of catalyst)

Catalyst	Efficiency (%)		Rate constant, k $\times$ 10^{-3}(min^{-1})			
	Acetaminophen	Caffeine	Acetaminophen	R^2	Caffeine	R^2
ZnO	15.8	13.8	1.4	0.97	1.2	0.98
CeO_2	12.7	12.7	1.2	0.97	1.2	0.97
g-C_3N_4	11.3	8.3	0.9	0.90	0.6	0.97
ZnO/CeO_2	18.0	15.5	1.6	0.97	1.4	0.98
ZnO/CeO_2/1.0CN	20.7	16.7	1.9	0.99	1.5	0.97
ZnO/CeO_2/1.5CN	27.1	20.9	2.4	0.94	1.8	0.95
ZnO/CeO_2/2.0CN	25.1	19.1	2.2	0.98	1.7	0.97
No catalyst	2.0	1.7	0.1	0.99	0.1	0.99

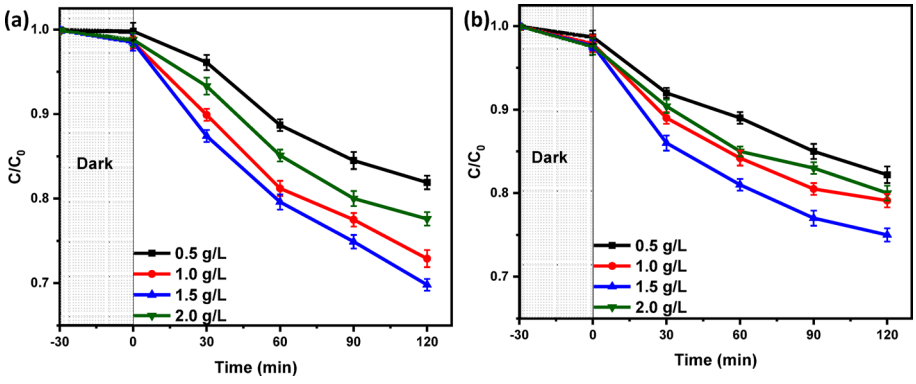

Fig. 11 Effect of the amount of ZnO/CeO_2/1.5CN in (**a**) acetaminophen and (**b**) caffeine photodegradation (Experimental conditions: Acetaminophen and caffeine concentration 10 µg/mL, pH 7)

1.0 gL^{-1}, 1.5 gL^{-1}, 2.0 gL^{-1}). From the results presented in Fig. 11, the catalyst amount affects photodegradation. Initially, the performance increased with the amount of catalyst raised from 0.5 gL^{-1} to 1.5 gL^{-1} which was associated with more active sites hence more hydroxyl (•OH) radical production at the irradiated catalyst surface [87]. However, a further increase to 2.0 gL^{-1} resulted in a reduced performance. This was attributed to the photocatalyst particles shielding photons from reaching particles inside the bulk solution as the amount was increased. Consequently, only the particles on the surface interacted with the photons and were actively involved in the photodegradation process. Additionally, the particles may have presumably agglomerated at high doses, lowering the available surface area and hence reducing performance [87, 88].

3.9.2 Effect of acetaminophen concentration

The acetaminophen and caffeine concentrations were varied from 10 µg/mL to 2 µg/mL considering their environmental concentrations. Figure 12 shows the performance. In both cases, the degradation of 10 µg/mL exhibited lower efficiencies which was attributed to the saturation of catalyst active sites at higher pollutant concentrations, which may have limited the generation of oxidizing species, in agreement with previous studies [87, 89, 90]. Another possible reason for low efficiencies at high concentrations is the competition between the intermediates and the primary acetaminophen molecules for the limited active sites [91, 92].

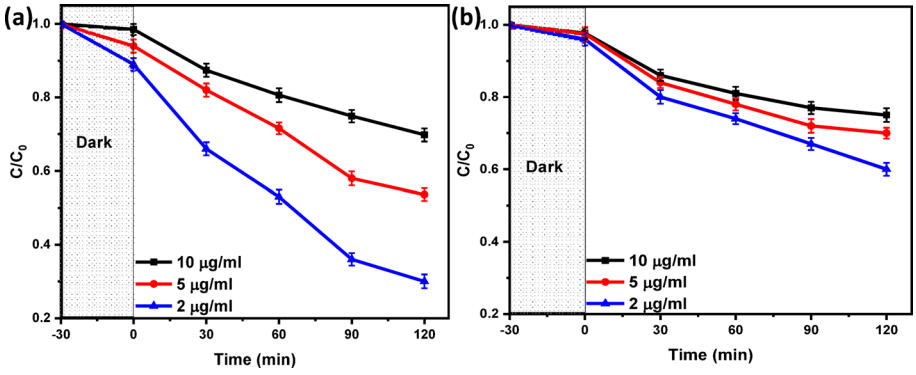

Fig. 12 Effect of initial concentration in (**a**) acetaminophen and (**b**) caffeine photodegradation in the presence of ZnO/CeO_2/1.5CN (Experimental conditions; catalyst dose 1.5 gL^{-1}, solution pH = 7)

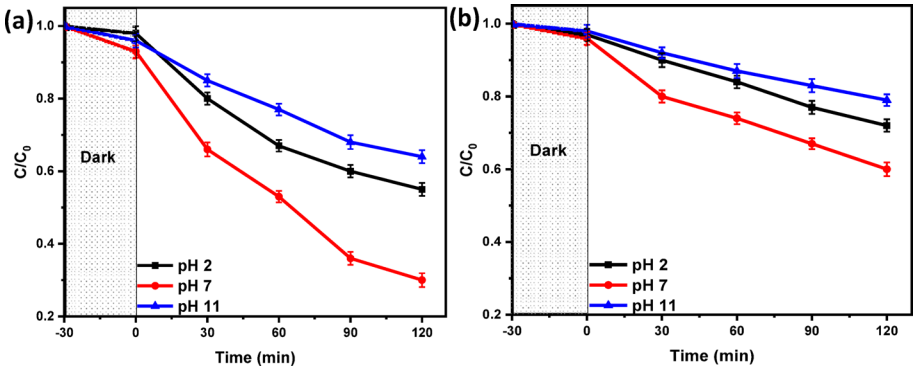

Fig. 13 The effect of initial pH on (**a**) acetaminophen and (**b**) caffeine photodegradation (Experimental conditions: Concentration 2 µg/mL, amount of catalyst 1.5 gL^{-1})

3.9.3 Effect of pH

The adsorption of acetaminophen and caffeine molecules on the photocatalyst surface is influenced by the surface charge determined by the solution's pH and the photocatalyst's zero-point charge (pH_{zpc}). A positive charge develops at the photocatalyst's surface when the solution pH < pH_{zpc}, and vice versa [93]. The zero-point charge of ZnO/CeO_2/g-C_3N_4 is 6.83 [35] indicating that it is neutral at pH = 6.83 and negatively charged at solution pH higher than 6.83. Acetaminophen whose acid ionization constant (pka) is 9.5 [91] is negatively charged when its solution pH is higher than 9.5. At neutral pH, acetaminophen exists in its non-ionic form and its adsorption on the catalyst surface is maximum since its water solubility is minimal [94]. From Fig. 13, the best performance at pH 7 was associated with hydroxyl ions formation on the photocatalyst surface. The repulsive electrostatic force between the acetaminophen and the photocatalyst resulted in minimal performance at high acetaminophen solution pH [87]. An enhanced acetaminophen photocatalytic degradation at weakly alkaline pH was reported earlier [95]. Caffeine degradation was also observed to be improved at neutral pH, ascribed to its pKa of 10.4, which makes it fully protonated at solution pH less than 10.4 [96], hence better adsorption compared to pH values equal to and greater than 10.4 where the caffeine molecules are neutral and less deprotonated respectively [97].

The decreased degradation at low pH in both pharmaceuticals was ascribed to unfavourable adsorption of the molecules on the photocatalyst surface. The acetaminophen

Table 4 (a): A comparison of acetaminophen photodegradation efficiency in this study with previous studies

Photocatalyst	Contaminant concentration (mg/L)	Irradiation type and time (min)	Performance efficiency (%)	Reference
$Cu_2O/WO_3/TiO_2$	1	Solar 60	92.50	[98]
g-C_3N_4-CdS/$Bi_4O_5I_2$	500	Visible 25	80.00	[99]
g-C_3N_4/CQD/Ag	50	UV Xenon 60	87.50 85.30	[100]
Zeolite/Fe_3O_4/CuS/$CuWO_4$	10	Solar 180	95.76	[101]
ZnO/CeO_2/g-C_3N_4	2	UV 120	70.00	This work

Table 5 A comparison of caffeine photodegradation efficiency in this study with previous studies

Photocatalyst	Contaminant concentration (mg/L)	Irradiation type and time (min)	Performance efficiency (%)	Reference
Ag-ZnO-Al_2O_3	20	UV 180	99.30	[97]
Mg-ZnO-Al_2O_3	20	UV 70	98.90	[96]
TiO_2/g-C_3N_4	20	UV 240	100	[102]
Cu/TiO_2-F NiO/TiO_2-F	25	UV 180	90.00 88.00	[103]
ZnO-$ZnAL_2O_4$	20	UV 90	97.32	[104]
ZnO/CeO_2/g-C_3N_4	2	UV 120	40.00	This work

and caffeine photodegradation efficiencies in the presence of ZnO/CeO_2/1.5CN nanocomposite at neutral pH were 70% and 40% respectively. The low efficiencies compared to other studies presented in Tables 4 and 5 may be attributed to the simultaneous photodegradation of the pharmaceuticals in one setup.

The performance efficiency with acetaminophen in our study was 70% (Table 4) and with caffeine was 40% (Table 5), which may indicate competitive interaction between the catalysts surface and the target degradation compounds during the simultaneous photodegradation.

3.9.4 Recyclability

To evaluate the reusability and recyclability of the ZnO/CeO_2/1.5CN nanocomposite, which demonstrated superior performance compared to the other nanocomposites, we used 1.5 gL^{-1} of the catalyst to degrade 2 µg/mL of acetaminophen and caffeine simultaneously. The same catalyst was employed throughout the experiment. After each use, the catalyst was recovered, washed, dried and then reused with a fresh solution of acetaminophen and caffeine. Figure 14 shows the degradation efficiencies over four repeated cycles. A slight decrease in the efficiencies was observed, attributed to the loss of photocatalyst powder during sampling and decanting. Despite this, the efficiencies remained stable indicating the catalyst's reliability.

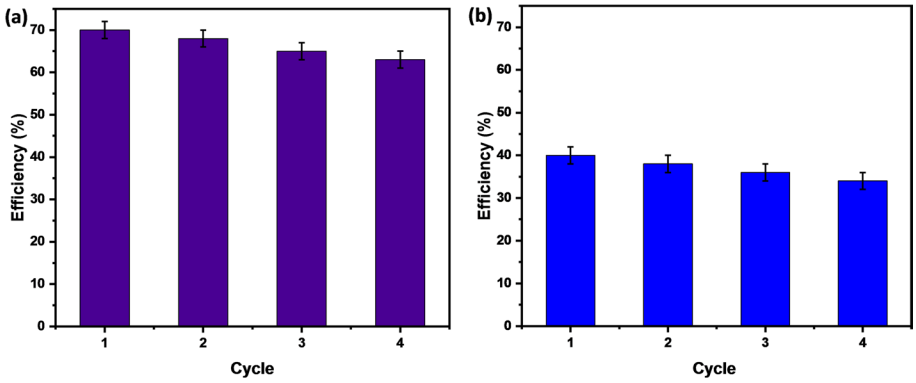

Fig. 14 Stability of the ZnO/CeO_2/g-C_3N_4 nanocomposite for the photo-degradation of (**a**) acetaminophen and (**b**) caffeine

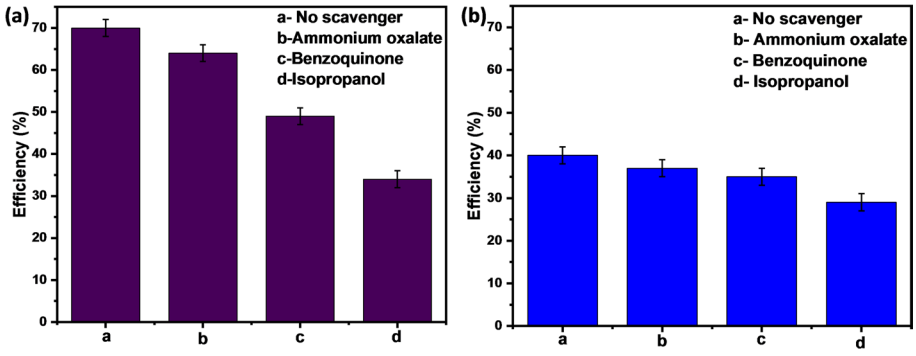

Fig. 15 Effect of scavengers on the photodegradation of (**a**) acetaminophen and (**b**) caffeine

3.10 Possible acetaminophen photodegradation mechanism

3.10.1 Reactive species

The role of reactive oxygen species in photodegradation was examined using 1 mM isopropanol, benzoquinone and ammonium oxalate to trap •OH, $O_2^{\bullet-}$ and h^+ respectively [105]. Figure 15 illustrates the impact of these scavengers on photodegradation efficiency. All scavengers caused quenching, but the variations in efficiency indicated that •OH radicals played the most significant role in the photodegradation process. Although $O_2^{\bullet-}$ and h^+ also contributed, their effects were less pronounced than those of •OH.

3.10.2 Proposed photodegradation mechanism

The possible transfer of the photogenerated charges used to propose the mechanism of the pharmaceutical degradation is elucidated in Fig. 16. The edge positions of the valence and conduction band were calculated using Mulliken's electronegativity equations [19].

$$E_{VB} = X - E_e + 0.5E_g \tag{9}$$

$$E_{CB} = E_{VB} - E_g \tag{10}$$

where X is the semiconductor's absolute electronegativity equal to 5.79 eV and 5.56 eV for ZnO and CeO_2 respectively [19] and 4.74 eV for g-C_3N_4 [35]. E_g is the band gap energy, E_e is the energy of the free electron on the Hydrogen scale always 4.5 eV, E_{VB} and E_{CB} are the valence band and conduction edges respectively.

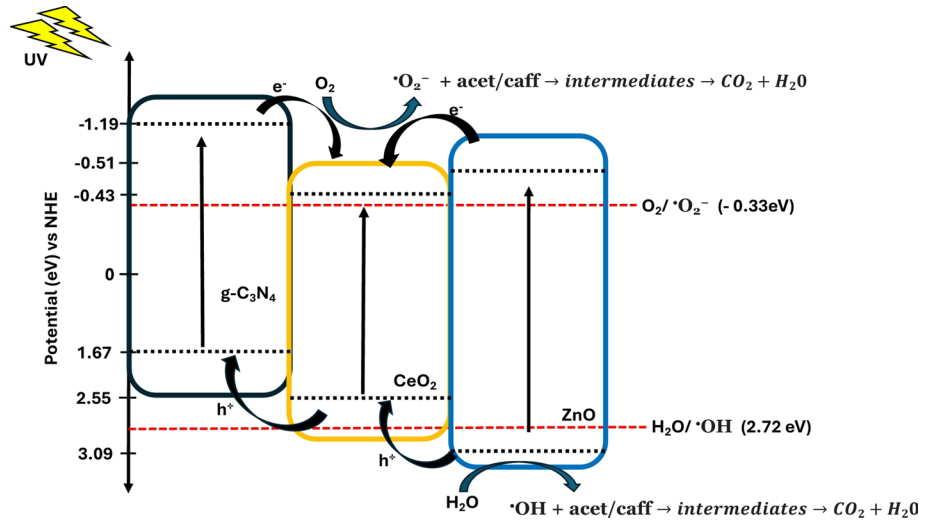

Fig. 16 Proposed charge transfer for acetaminophen and caffeine photodegradation using ZnO/CeO_2/g-C_3N_4 ternary nanocomposite photocatalyst

The calculated valence and conduction band edges for the ZnO, CeO_2 and g-C_3N_4 were 3.09 eV, 2.55 eV, 1.67 eV and − 0.51 eV, −0.43 eV, −1.18 eV, respectively, as indicated in Fig. 16. During photodegradation, the UV radiation excited electrons from the valence bands of all the semiconductors. The electrons in the g-C_3N_4 and ZnO conduction bands moved to the CeO_2 conduction band to align their Fermi levels. At the same time, the holes moved from the ZnO valence band to CeO_2 and then g-C_3N_4 valence bands due to the potential difference, promoting charge separation. It is important to note that O_2 can be reduced to superoxide radical ion and H_2O oxidized to hydroxyl radical if the semiconductor conduction band position is more negative than the O_2 reduction potential and the valence band is more positive than the H_2O oxidation potential [106]. Superoxide ($O_2^{\bullet-}$) radicals were formed in all the semiconductor conduction bands since their conduction band potentials are higher than the $O_2/O_2^{\bullet-}$ standard redox potential (−0.33 eV) [107], although the superoxides did not play a major role in photodegradation as revealed by the scavenger tests. Also, only the holes in the ZnO valence band formed hydroxyl (•OH) radicals since its valence band potential is higher than •OH/H_2O redox potential (2.72 eV) [107]. Holes can directly oxidize surface-adsorbed molecules [108]. The reactive radicals formed and the holes mineralized the contaminants into simpler compounds (intermediates) and finally into water and carbon dioxide. Whereas the arrangement in Fig. 16 demonstrated improved charge separation, a limited number of generated radicals may have led to the low efficiencies observed in the simultaneous degradation of the pharmaceuticals. We recommend further studies on the performance of the nanocomposite in the simultaneous photodegradation of the pharmaceuticals in the presence of electron acceptors such as H_2O_2 or persulfate to boost the production of the reactive oxygen species.

Overall, the current study used a commercial visible light lamp with some UV-A output, and relatively low power output. Future work on using the catalysts with a suitable prototype reactor in direct sunlight would be of interest for real world applications, and may allow for degradation of more challenging and complex mixtures.

4 Conclusion

A hydrothermal method was adapted to synthesize a $ZnO/CeO_2/g\text{-}C_3N_4$ ternary nanocomposite. Comparative analysis of the ternary nanocomposite to its components synthesized using a similar hydrothermal method was done using powder-XRD, FTIR, SEM, XPS and TEM. Morphological, surface area analysis, optical and structural characterization indicated their crystallinity and purity, an improved specific surface area, absorption and charge separation. XPS analysis confirmed the presence of Zn, Ce, O, C and N elements in the nanocomposite. From SEM and TEM analysis, ZnO nanoflowers were formed and changed to spheres when CeO_2 was introduced which interacted well with $g\text{-}C_3N_4$. An augmented photodegradation performance towards acetaminophen and caffeine photodegradation was obtained with the nanocomposites than with pristine ZnO with $ZnO/CeO_2/1.5CN$ achieving 70% and 40% of 2 µg/mL acetaminophen and caffeine photodegradation in 120 min under UV-A irradiation respectively. The nanocomposite portrayed good recyclability and stability after 4 cycles hence their potential for environmental remediation application. The proposed mechanism for pharmaceutical photodegradation was presented.

Supplementary Information

The online version contains supplementary material available at https://doi.org/10.1007/s42452-025-07598-7.

Supplementary Material 1

Acknowledgements
The authors are grateful for the research support received from the University of Pretoria. J Chebwogen acknowledges PASET, an Africa-led, World Bank-affiliated initiative for a Regional Scholarship and Innovation Fund (RSIF) for providing a bursary to pursue her PhD studies.

Author contributions
J.C. Conceptualization, Methodology, Formal analysis, Investigation, Writing - Original Draft. F.W.N. Writing - Review & Editing, Supervision, Project administration, Funding acquisition. J.M.M. Writing - Review & Editing, Supervision, Project administration, Funding acquisition. P.G.N. Validation, Formal analysis, Writing - Review & Editing, Visualisation, Supervision, Project administration, Funding acquisition.

Funding
This work was partially funded by The Faculty of Natural and Agricultural Sciences at the University of Pretoria, and the Partnership for Skill in Applied Sciences, Engineering and Technology (PASET), an Africa-led, World Bank-affiliated initiative.

Data availability
The authors declare that the data supporting the findings of this study are available within the paper.

Declarations

Ethics and consent to participate
Not Applicable.

Consent to publish
Not Applicable.

Competing interest
The authors declare no competing interests.

Received: 18 April 2025 / Accepted: 5 August 2025
Published online: 22 October 2025

References

1. Sarker B, Keya KN, Mahir FI, Nahiun KM, Shahida S, Khan RA. Surface and ground water pollution: causes and effects of urbanization and industrialization in South Asia. Sci Rev. 2021;7(3):32–41.
2. Sarkar S, Ponce NT, Banerjee A, Bandopadhyay R, Rajendran S, Lichtfouse E. Green polymeric nanomaterials for the photocatalytic degradation of dyes: a review. Environ Chem Lett. 2020;18(5):1569–80.

3. Samal K, Mahapatra S, Hibzur M, Ali. Pharmaceutical wastewater as emerging contaminants (EC): treatment technologies, impact on environment and human health. Energy Nexus. 2022;6:100076.
4. Velempini T, Prabakaran E, Pillay K. Recent developments in the use of metal oxides for photocatalytic degradation of pharmaceutical pollutants in water—a review. Mater Today Chem. 2021;19: 100380.
5. Patel M, Kumar R, Kishor K, Mlsna T, Pittman CU Jr., Mohan D. Pharmaceuticals of emerging concern in aquatic systems: chemistry, occurrence, effects, and removal methods. Chem Rev. 2019;119(6):3510–673.
6. Hawash HB, Moneer AA, Galhoum AA, Elgarahy AM, Mohamed WAA, Samy M, El-Seedi HR, Gaballah MS, Mubarak MF, Attia NF. Occurrence and spatial distribution of pharmaceuticals and personal care products (PPCPs) in the aquatic environment, their characteristics, and adopted legislations. J Water Process Eng. 2023;52: 103490.
7. Wang H, Xi H, Xu L, Jin M, Zhao W, Liu H. Ecotoxicological effects, environmental fate and risks of pharmaceutical and personal care products in the water environment: a review. Sci Total Environ. 2021;788: 147819.
8. Phong Vo HN, Le GK, Hong Nguyen TM, Bui X-T, Nguyen KH, Rene ER, Vo TDH, Thanh Cao N-D, Mohan R. Acetaminophen micropollutant: historical and current occurrences, toxicity, removal strategies and transformation pathways in different environments. Chemosphere. 2019;236:124391.
9. Peralta-Hernández JM, Brillas E. A critical review over the removal of Paracetamol (acetaminophen) from synthetic waters and real wastewaters by direct, hybrid catalytic, and sequential ozonation processes. Chemosphere. 2023;313:137411.
10. Lee WJ, Goh PS, Lau WJ, Ismail AF. Removal of pharmaceutical contaminants from aqueous medium: a state-of-the-art review based on Paracetamol. Arab J Sci Eng. 2020;45(9):7109–35.
11. Li S, Wen J, He B, Wang J, Hu X, Liu J. Occurrence of caffeine in the freshwater environment: implications for ecopharmacovigilance. Environ Pollut. 2020;263: 114371.
12. Sathish S, Supriya S, Aravind kumar J, Prabu D, Marshiana D, Rajasimman M, Vasseghian Y. Enhanced photocatalytic degradation of caffeine using Co–Zn/Al2O3 nanocomposite. Chemosphere. 2022;307:135773.
13. Ghosh M, Manoli K, Shen X, Wang J, Ray AK. Solar photocatalytic degradation of caffeine with titanium dioxide and zinc oxide nanoparticles. J Photochem Photobiol A. 2019;377:1–7.
14. Yang X, Sun H, Li G, An T, Choi W. Fouling of TiO2 induced by natural organic matters during photocatalytic water treatment: mechanisms and regeneration strategy. Appl Catal B. 2021;294: 120252.
15. Ameta SC, Ameta R. Advanced oxidation processes for wastewater treatment: emerging green chemical technology. Academic; 2018.
16. Ma D, Yi H, Lai C, Liu X, Huo X, An Z, Li L, Fu Y, Li B, Zhang M. Critical Rev Adv Oxidation Processes Org Wastewater Treat Chemosphere. 2021;275:130104.
17. Sawunyama L, Oyewo O, Onwudiwe DC, Makgato SS. Photocatalytic degradation of tetracycline using surface defective black TiO2–ZnO heterojunction photocatalyst under visible light. Heliyon. 2023. https://doi.org/10.1016/j.heliyon.2023.e21423.
18. Mirikaram N, Pérez-Molina Á, Morales-Torres S, Salemi A, Maldonado-Hódar FJ, Pastrana-Martínez LM. Photocatalytic performance of ZnO-graphene oxide composites towards the degradation of vanillic acid under solar radiation and visible-LED. Nanomaterials. 2021;11(6):1576.
19. Das A, Patra M, Bhagavathiachari M, Nair RG. Defect-induced visible-light-driven photocatalytic and photoelectrochemical performance of ZnO–CeO2 nanoheterojunctions. J Alloys Compd. 2021;858: 157730.
20. Nayan M, Krishnegowda J, Abhilash M, Keerthiraj DN, Shivanna S. Comparative Study on the Effects of Surface Area, Conduction Band and Valence Band Positions on the Photocatalytic Activity of ZnO-M_xO_y Heterostructures. Journal of Water Resource and Protection. 2019;11:357–70.
21. Liu G, Wang H, Chen D, Dai C, Zhang Z, Feng Y. Photodegradation performances and transformation mechanism of sulfamethoxazole with CeO2/CN heterojunction as photocatalyst. Sep Purif Technol. 2020;237: 116329.
22. Tuan TQ, Van Huan P, Hoan BT, Van HN, Hung DD, Trung NN, Nghia HA, Hoa ND, Tam PD, Pham V-H. Enhanced photocatalytic activity of C-doped CeO2 nanoparticles under visible light irradiation for degradation of methylene blue. J Appl Spectrosc. 2023;90(5):1114–22.
23. Xiao Y, Yu H, Dong X-t. Ordered mesoporous CeO2/ZnO composite with photodegradation concomitant photocatalytic hydrogen production performance. J Solid State Chem. 2019;278: 120893.
24. Nallusamy S, Asaithambi S, Pandiaraj S, Rahaman M, Elangovan V, Eswaramoorthy N, Nandagopal C. Cerium-modified TiO2/g-C3N4 nanocomposites with synergistic effect on enhancing visible-light photocatalytic activity employing cationic dyes. Colloids Surf A Physicochem Eng Asp. 2024;685: 133175.
25. Manikanika L, Chopra Kumar, Kumar R. Combustion-synthesized ZnO-CeO2 heterojunctions for advanced photocatalytic dye degradation. Inorg Chem Commun. 2024;160: 111896.
26. Luo X, Dong Y, Wang D, Duan Y, Lei K, Mao L, Li Y, Zhao Q, Sun Y. Facile synthesis of g-C3N4 nanosheets for effective degradation of organic pollutants via ball milling. Rev Adv Mater Sci. 2023;62(1): 20230123.
27. Bandoh CK, Haruna M, Adu-Poku D, Danu BY, Pinto O, Toku M, Badu M, Agorku ES, Ampong FK, Nkum RK. Gd-doped ZnO-g-C3N4 nanocomposite: a novel photocatalyst for the photodegradation of eosin yellow dye in water. Discover Appl Sci. 2025;7(4): 272.
28. Yang X, Zhao L, Wang S, Li J, Chi B. Recent progress of g-C3N4 applied in solar cells. J Materiomics. 2021;7(4):728–41.
29. Zhu Z, Lu Z, Wang D, Tang X, Yan Y, Shi W, Wang Y, Gao N, Yao X, Dong H. Construction of high-dispersed Ag/Fe3O4/g-C3N4 photocatalyst by selective photo-deposition and improved photocatalytic activity. Appl Catal B. 2016;182:115–22.
30. Gao X, Yang B, Yao W, Wang Y, Zong R, Wang J, Li X, Jin W, Tao D. Enhanced photocatalytic activity of ZnO/g-C3N4 composites by regulating stacked thickness of g-C3N4 nanosheets. Environ Pollut. 2020;257:113577.
31. Taufik A, Albert A, Saleh R. Sol-gel synthesis of ternary CuO/TiO2/ZnO nanocomposites for enhanced photocatalytic performance under UV and visible light irradiation. J Photochem Photobiol A. 2017;344:149–62.
32. Muñoz-Batista MJ, Fernández-García M, Kubacka A. Promotion of CeO2–TiO2 photoactivity by g-C3N4: ultraviolet and visible light elimination of toluene. Appl Catal B. 2015;164:261–70.
33. Akhundi A, Habibi-Yangjeh A. Ternary g-C3N4/ZnO/AgCl nanocomposites: synergistic collaboration on visible-light-driven activity in photodegradation of an organic pollutant. Appl Surf Sci. 2015;358:261–9.
34. Yuan Y, Huang G-F, Hu W-Y, Xiong D-N, Zhou B-X, Chang S, Huang W-Q. Construction of g-C3N4/CeO2/ZnO ternary photocatalysts with enhanced photocatalytic performance. J Phys Chem Solids. 2017;106:1–9.

35. Girma S, Taddesse AM, Bogale Y, Bezu Z. Zeolite-supported g-C3N4/ZnO/CeO2 nanocomposite: synthesis, characterization and photocatalytic activity study for methylene blue dye degradation. J Photochem Photobiol A Chem. 2023;444: 114963.
36. Ahmad T, Pandey V, Saddam Husain M, Adiba, Munjal S. Structural and spectroscopic analysis of pure phase hexagonal wurtzite ZnO nanoparticles synthesized by sol-gel. Materials Today: Proceedings. 2022;49:1694–7.
37. Ayon SA, Billah MM, Nishat SS, Kabir A. Enhanced photocatalytic activity of Ho3+ doped ZnO NPs synthesized by modified sol-gel method: an experimental and theoretical investigation. J Alloys Compd. 2021;856: 158217.
38. Manikanika L, Chopra, Kumar R. Photocatalytic degradation efficiencies of ZnO nanoparticles and CeO2 nanosheets synthesized via combustion method. Bull Mater Sci. 2023;46(3):181.
39. Pathak V, Lad P, Thakkar AB, Thakor P, Deshpande MP, Pandya S. Synthesis, characterization and applications of cubic fluorite cerium oxide nanoparticles: a comprehensive study. Results Surf Interfaces. 2023;11: 100111.
40. Zhao S, Jiang J, Zhang C, Chen F, Song Y, Tang Y. Construction of a novel double S-scheme heterojunction CeO2/g-C3N4/Bi2O4 for significantly boosted degradation of tetracycline: insight into the dual charge transfer mode. Chem Eng J. 2024;479: 147333.
41. Ngullie RC, Alaswad SO, Bhuvaneswari K, Shanmugam P, Pazhanivel T, Arunachalam P. Synthesis and characterization of efficient ZnO/g-C3N4 nanocomposites photocatalyst for photocatalytic degradation of methylene blue. Coatings. 2020;10(5):500.
42. Swathi A, Sandhiya S, Sreelakshmi B, Chandran M. Precursor dependent-visible light-driven g-C3N4 coated polyurethane foam for photocatalytic applications. Chemosphere. 2024;350:141013.
43. Gupta SV, Kulkarni VV, Ahmaruzzaman M. ZIF-8 incorporated CeO2-CdS quantum dots @ 2D g-C3N4 nanosheets as a staggered type II heterojunction for decolouration of a set of dyes. J Environ Chem Eng. 2024;12(1): 111642.
44. Scherrer P. Bestimmung der grosse und inneren struktur von kolloidteilchen mittels Rontgenstrahlen. Nachr Ges Wiss Goettingen. 1918;2:8–100.
45. Deng Y, Li Q, Wang P, Sun F, Li C, Li R. Crystal size dependent photogenerated charge separation on an octahedral bismuth vanadate photocatalyst. Catal Sci Technol. 2024;14(15):4228–35.
46. Bulcha B, Leta Tesfaye J, Anatol D, Shanmugam R, Dwarampudi LP, Nagaprasad N, Bhargavi VLN, Krishnaraj R. Synthesis of Zinc Oxide Nanoparticles by Hydrothermal Methods and Spectroscopic Investigation of Ultraviolet Radiation Protective Properties. Journal of Nanomaterials, 2021;p. 8617290.
47. Vashistha I, Rohilla S. Structural characterization and rietveld refinement of CeO2/CoFe2O4 nanocomposites prepared via coprecipitation method. IOP Conf Ser Mater Sci Eng. 2020;872(1): 012170.
48. Bhosale A, Gophane A, Kadam J, Sabale S, Sonawane K, Garadkar K. Fabrication of visible-active ZnO-gC3N4 nanocomposites for photodegradation and cytotoxicity of Methyl orange and antibacterial activity towards drug resistance pathogens. Opt Mater. 2023;136: 113392.
49. Jayapandi S, Premkumar S, Lakshmi D, Packiyaraj P, Balaji viswanath K, Sivaraj P, Anitha K. Reinforced photocatalytic reduction of SnO2 nanoparticle by La incorporation for efficient photodegradation under visible light irradiation. J Mater Sci Mater Electron. 2019;30(9):8479–92.
50. Abass A, Karim A, Al-Sammarraie M. Chemical Methodologies Synthesis of New PbO-Fe2O3-Polypyrrole Hybrid Nanocomposite to Improve the Structural, Magnetic and Electrical Characteristics of Lead Oxide. 2022: pp. 301–318.
51. Ahmed M, Abd-Elhamid M, Sarhan A, Hassan A. Preparation and characterization of ZnO nanoparticles by simple precipitation method. Int J Sci Eng Technol. 2016;4(3):507–12.
52. Anwar A, Ma'amor A, Mahmud HE, Basirun WJ, Abdullah I. Catalytic activity of ethylbenzene with product selectivity by gold nanoparticlessupported on zinc oxide. Turk J Chem. 2022;46(3):730–46.
53. Miao Y, Zhang H, Yuan S, Jiao Z, Zhu X. Preparation of flower-like ZnO architectures assembled with nanosheets for enhanced photocatalytic activity. J Colloid Interface Sci. 2016;462:9–18.
54. Syed A, Yadav LSR, Bahkali AH, Elgorban AM, Abdul Hakeem D, Ganganagappa N. Effect of CeO2-ZnO nanocomposite for photocatalytic and antibacterial activities. Crystals. 2020;10(9):817.
55. Jung H, Pham T-T, Shin EW. Interactions between ZnO nanoparticles and amorphous g-C3N4 nanosheets in thermal formation of g-C3N4/ZnO composite materials: the annealing temperature effect. Appl Surf Sci. 2018;458:369–81.
56. Xing Z, Chen Y, Liu C, Yang J, Xu J, Situ Y, Huang H. Synthesis of core-shell ZnO/oxygen doped g-C3N4 visible light driven photocatalyst via hydrothermal method. J Alloys Compd. 2017;708:853–61.
57. Liu L, Luo X, Li Y, Xu F, Gao Z, Zhang X, Song Y, Xu H, Li H. Facile synthesis of few-layer g-C3N4/ZnO composite photocatalyst for enhancing visible light photocatalytic performance of pollutants removal. Colloids Surf A Physicochem Eng Asp. 2018;537:516–23.
58. Goktas S, Goktas A. A comparative study on recent progress in efficient ZnO based nanocomposite and heterojunction photocatalysts: a review. J Alloys Compd. 2021;863: 158734.
59. Sahu K, Kar AK. Morphological, optical, photocatalytic and electrochemical properties of hydrothermally grown ZnO nanoflowers with variation in hydrothermal temperature. Mater Sci Semicond Process. 2019;104: 104648.
60. Zhang H, Yang D, Li S, Ma X, Ji Y, Xu J, Que D. Controllable growth of ZnO nanostructures by citric acid assisted hydrothermal process. Mater Lett. 2005;59(13):1696–700.
61. Mohamed NA, Safaei J, Ismail AF, Mohamad Noh MF, Arzaee NA, Mansor NN, Ibrahim MA, Ludin NA, Sagu JS. Mat teridi, Fabrication of exfoliated graphitic carbon nitride, (g-C3N4) thin film by methanolic dispersion. J Alloys Compd. 2020;818:152916.
62. Thommes M, Kaneko K, Neimark AV, Olivier JP, Rodriguez-Reinoso F, Rouquerol J, Sing KSW. Physisorption of gases, with special reference to the evaluation of surface area and pore size distribution (IUPAC technical Report). Pure Appl Chem. 2015;87(9–10):1051–69.
63. Vardast N, Haghighi M, Zeinalzadeh H. Catalytic properties/performance evolution during sono-hydrothermal design of nanocrystalline ceria over zinc oxide for biofuel production. Chem Eng J. 2022;430: 132764.
64. Ren L, Tao Y, Ma S, Liu Z, Yang M, Wang S, Gao Z, Xie H. Controllable preparation and photocatalytic activity of hierarchical flower-like microspheres clustered by ZnO porous nanosheets. Chem Phys. 2022;559: 111552.
65. Kumar A, Navakoteswara Rao V, Kumar A, Venkatakrishnan Shankar M, Krishnan V. Interplay between mesocrystals of CaTiO3 and edge sulfur atom enriched MoS2 on reduced graphene oxide nanosheets: enhanced photocatalytic performance under sunlight irradiation. ChemPhotoChem. 2020;4(6):427–44.

66. Kumar S, Ahmed F, Shaalan NM, Saber O. Biosynthesis of CeO2 nanoparticles using egg white and their antibacterial and antibiofilm properties on clinical isolates. Crystals. 2021;11(6):584.
67. Umar A, Akhtar MS, Al-Hajry A, Al-Assiri MS, Almehbad NY. Hydrothermally grown ZnO nanoflowers for environmental remediation and clean energy applications. Mater Res Bull. 2012;47(9):2407–14.
68. Tauc J, Grigorovici R, Vancu A. Optical properties and electronic structure of amorphous germanium. physica status solidi (b). 1966;15(2):627–37.
69. Makuła P, Pacia M, Macyk W. How to correctly determine the band gap energy of modified semiconductor photocatalysts based on UV–Vis spectra. J Phys Chem Lett. 2018;9(23):6814–7.
70. Rostami M, Badiei A. Molten salt-shielded preparation of the ultrathin nanosheets of Ti3C2Cl2 @TiO2 coupled with Fe3O4@C-C3N4 for assessing photocatalytic activity. Ceram Int. 2024;50(8):13608–20.
71. Meenakshi G, Sivasamy A. Enhanced photocatalytic activities of CeO2@ZnO core-shell nanostar particles through delayed electron hole recombination process. Colloids Surf A Physicochem Eng Asp. 2022;645: 128920.
72. Anbalagan Ak, Gupta S, kumar A, Haw S-C, Kulkarni SS, Tai N-H, Tseng F-G, Hwang KC, Lee C-H. Gamma ray irradiation enhances the linkage of cotton fabrics coated with ZnO nanoparticles. ACS Omega. 2020;5(25):15129–35.
73. Phor L, Ankush, Suman J, Malik S, Sharma, Sonia V, Chaudhary GM, Rani A, Kumar P, Kumar, Chahal S. Magnetically separable NiZn-ferrite/CeO2 nanorods/cnt ternary composites for photocatalytic removal of organic pollutants. J Mol Liq. 2023;390:123064.
74. Ujjain SK, Das A, Srivastava G, Ahuja P, Roy M, Arya A, Bhargava K, Sethy N, Singh SK, Sharma RK, Das M. Nanoceria based electrochemical sensor for hydrogen peroxide detection. Biointerphases. 2014. https://doi.org/10.1116/1.4890473.
75. Idriss H. On the wrong assignment of the XPS O1s signal at 531–532 eV attributed to oxygen vacancies in photo- and electro-catalysts for water splitting and other materials applications. Surf Sci. 2021;712: 121894.
76. Djaouida A, Smain H, Sébastien T, Ksenia P, Anne-Cécile R, Samira K. Comparative study on the effect of Cerina and alumina on the catalytic activity of CuO-ZnO based catalyst in CO2 hydrogenation to methanol. Catal Lett. 2024;154(11):5849–64.
77. Gong S, Jiang Z, Zhu S, Fan J, Xu Q, Min Y. The synthesis of graphene-TiO2/g-C3N4 super-thin heterojunctions with enhanced visible-light photocatalytic activities. J Nanopart Res. 2018;20(11):310.
78. Qu Y, Huang R, Qi W, Shi M, Su R, He Z. Controllable synthesis of ZnO nanoflowers with structure-dependent photocatalytic activity. Catal Today. 2020;355:397–407.
79. Qiao Q, Yang K, Ma L-L, Huang W-Q, Zhou B-X, Pan A, Hu W, Fan X, Huang G-F. Facile in situ construction of mediator-free direct Z-scheme g-C3N4/CeO2 heterojunctions with highly efficient photocatalytic activity. J Phys D Appl Phys. 2018;51(27): 275302.
80. Xing H, Ma H, Fu Y, Xue M, Zhang X, Dong X, Zhang X. Preparation of g-C3N4/ZnO composites and their enhanced photocatalytic activity. Mater Technol. 2015;30(2):122–7.
81. Shen H, Shi X, Wang Z, Hou Z, Xu C, Duan L, Zhao X, Wu H. Defects control and origins of blue and green emissions in sol-gel ZnO thin films. Vacuum. 2022;202:111201.
82. Paul DR, Gautam S, Panchal P, Nehra SP, Choudhary P, Sharma A. ZnO-Modified g-C3N4: A potential photocatalyst for environmental application. ACS Omega. 2020;5(8):3828–38.
83. Guan R, Li J, Zhang J, Zhao Z, Wang D, Zhai H, Sun D. Photocatalytic performance and mechanistic research of ZnO/g-C3N4 on degradation of methyl orange. ACS Omega. 2019;4(24):20742–7.
84. Camarda P, Messina F, Vaccaro L, Agnello S, Buscarino G, Schneider R, Popescu R, Gerthsen D, Lorenzi R, Gelardi FM, Cannas M. Luminescence mechanisms of defective ZnO nanoparticles. Phys Chem Chem Phys. 2016;18(24):16237–44.
85. Sherly ED, Vijaya JJ, Kennedy LJ. Effect of CeO2 coupling on the structural, optical and photocatalytic properties of ZnO nanoparticle. J Mol Struct. 2015;1099:114–25.
86. Fernandes TA, Mendo SG, Ferreira LP, Neng NR, Oliveira MC, Gil A, Carvalho MD, Monteiro OC, Nogueira JMF, Calhorda MJ. Photocatalytic degradation of acetaminophen and caffeine using magnetite–hematite combined nanoparticles: kinetics and mechanisms. Environ Sci Pollut Res. 2021;28(14):17228–43.
87. Dalida MLP, Amer KMS, Su C-C, Lu M-C. Photocatalytic degradation of acetaminophen in modified TiO2 under visible irradiation. Environ Sci Pollut Res. 2014;21(2):1208–16.
88. Karthika V, Karthikeyan S, Kathirvel R. Photocatalytic degradation of acetaminophen, ciprofloxacin and amoxicillin using UV/ZnO in a suspended photocatalytic reactor. Phys Scr. 2024;99(11):115930. https://doi.org/10.1088/1402-4896/ad804a
89. Castro-Campoy D, Vargas-Hernández D, Sánchez-Cruz M, Hernández-Huesca R. Photodegradation of acetaminophen and ibuprofen in iron supported in SBA-15 under UV irradiation. J Photochem Photobiol A Chem. 2023;441: 114716.
90. Muangmora R, Kemacheevakul P, Punyapalakul P. Chuangchote. Enhanced photocatalytic degradation of caffeine using titanium dioxide photocatalyst immobilized on circular glass sheets under ultraviolet C irradiation. Catalysts. 2020;10. https://doi.org/10.3390/catal10090964.
91. Chijioke-Okere MO, Adlan Mohd Hir Z, Ogukwe CE, Njoku PC, Abdullah AH, Oguzie EE. TiO2/Polyethersulphone films for photocatalytic degradation of acetaminophen in aqueous solution. J Mol Liq. 2021;338:116692.
92. Ramasamy B, Jeyadharmarajan J, Chinnaiyan P. Novel organic assisted Ag-ZnO photocatalyst for Atenolol and acetaminophen photocatalytic degradation under visible radiation: performance and reaction mechanism. Environ Sci Pollut Res. 2021;28(29):39637–47.
93. Hanafi MF, Sapawe N. Influence of pH on the photocatalytic degradation of Methyl orange using nickel catalyst. Mater Today Proc. 2020;31:339–41.
94. Jallouli N, Elghniji K, Trabelsi H, Ksibi M. Photocatalytic degradation of Paracetamol on TiO2 nanoparticles and TiO2/cellulosic fiber under UV and sunlight irradiation. Arab J Chem. 2017;10:S3640–5.
95. Nasr O, Mohamed O, Al-Shirbini A-S, Abdel-Wahab A-M. Photocatalytic degradation of acetaminophen over Ag, Au and Pt loaded TiO2 using solar light. J Photochem Photobiol A Chem. 2019;374:185–93.
96. Elhalil A, Elmoubarki R, Farnane M, Machrouhi A, Sadiq M, Mahjoubi FZ, Qourzal S, Barka N. Photocatalytic degradation of caffeine as a model pharmaceutical pollutant on Mg doped ZnO-Al2O3 heterostructure. Environ Nanotechnol Monit Manag. 2018;10:63–72.
97. Elhalil A, Elmoubarki R, Sadiq Mh, Abdennouri M, Kadmi Y, Favier L, Qourzal S, Barka N. Enhanced photocatalytic degradation of caffeine as a model pharmaceutical pollutant by Ag-ZnO-Al2O3 nanocomposite. Desalination Water Treat. 2017;94:254–62.

98. Chau JHF, Lai CW, Leo BF, Juan JC, Johan MR. Advanced photocatalytic degradation of acetaminophen using Cu2O/WO3/TiO2 ternary composite under solar irradiation. Catal Commun. 2022;163: 106396.
99. Li K, Chen J, Ao Y, Wang P. Preparation of a ternary g-C3N4-CdS/Bi4O5I2 composite photocatalysts with two charge transfer pathways for efficient degradation of acetaminophen under visible light irradiation. Sep Purif Technol. 2021;259: 118177.
100. Toolabi A, Tahergorabi M, Mehralipour J, Seyedi N. Nasseh *Photocatalytic Degradation of Acetaminophen by g-C3N4/CQD/Ag Nanocomposites from Aqueous Media*. J Compos Sci. 2025. https://doi.org/10.3390/jcs9050197.
101. Ali AH, Alwared AI. Solar-photocatalytic degradation of paracetamol using Zeolite/Fe3O4/CuS/CuWO4 p-n heterojunction: synthesis, characterization and its application. Solar Energy. 2025;290: 113383.
102. Md Fauzi MAF, Hasmizam RM, Uwaisulqarni OM, and B. and, Azam M. Synthesis and characterisation of TiO2/g-C3N4 as photocatalyst for photodegradation of dyes, phenol and caffeine. Adv Mater Process Technol. 2022;8(4):4395–415.
103. Castañeda C, Martínez JJ, Santos L, Rojas H, Osman SM, Gómez R, Luque R. Caffeine photocatalytic degradation using composites of NiO/TiO2–F and CuO/TiO2–F under UV irradiation. Chemosphere. 2022;288:132506.
104. Elhalil A, Elmoubarki R, Machrouhi A, Sadiq M, Abdennouri M, Qourzal S, Barka N. Photocatalytic degradation of caffeine by ZnO-ZnAl2O4 nanoparticles derived from LDH structure. J Environ Chem Eng. 2017;5(4):3719–26.
105. Liu W, Wang M, Xu C, Chen S, Fu X. Significantly enhanced visible-light photocatalytic activity of g-C3N4 via ZnO modification and the mechanism study. J Mol Catal A: Chem. 2013;368–369:9–15.
106. Sagadevan S, Alshahateet SF, Lett JA, Fatimah I, Sivasankaran RP, Sibhatu AK, Leonard E, Le M-V, Soga T. Highly efficient photocatalytic degradation of methylene blue dye over Ag_2O nanoparticles under solar light irradiation. Inorg Chem Commun. 2023;148: 110288.
107. Wei K, Wang B, Hu J, Chen F, Hao Q, He G, Wang Y, Li W, Liu J, He Q. Photocatalytic properties of a new Z-scheme system BaTiO 3/in 2 S 3 with a core–shell structure. RSC Adv. 2019;9(20):11377–84.
108. Yuan L, Qi MY, Tang ZR, Xu YJ. Coupling strategy for CO2 valorization integrated with organic synthesis by heterogeneous photocatalysis. Angew Chem. 2021;133(39):21320–42.

Publisher's note